

Research paper

PhysRFANet: Physics-guided neural network for real-time prediction of thermal effect during radiofrequency ablation treatment

Minwoo Shin^a, Minjee Seo^a, Seonaeng Cho^a, Juil Park^b, Joon Ho Kwon^b, Deukhee Lee^{c,d}, Kyungho Yoon^{a,*}^a Yonsei University, School of Mathematics and Computing (Computational Science and Engineering), Seoul, 03722, Republic of Korea^b Yonsei University College of Medicine, Department of Radiology, Seoul, 03722, Republic of Korea^c Center for Healthcare Robotics, Korea Institute of Science and Technology, Seoul, 02792, Republic of Korea^d Yonsei University, Yonsei-KIST Convergence Research Institute, Seoul, 03722, Republic of Korea

ARTICLE INFO

Dataset link: <https://github.com/iangilan/PhysRFANet>

Keywords:

Radiofrequency ablation

Ablation lesion

Computer simulation

Deep learning

Convolutional neural network

Attention U-net

ABSTRACT

Radiofrequency ablation (RFA) is a minimally invasive technique that is widely used to ablate solid tumors. Achieving precise personalized treatment requires feedback information on *in situ* thermal effects induced by RFA. Although computer simulations facilitate the prediction of electrical and thermal phenomena associated with RFA, their practical implementation in clinical settings is hindered by their high computational demands. In this paper, we propose a physics-guided radiofrequency ablation neural network (PhysRFANet) to enable real-time prediction of thermal effect during RFA treatment. Three networks, an encoder-decoder based convolutional neural network (EDCNN), U-Net, and attention U-Net, designed for predicting the temperature distribution and the corresponding ablation lesion, were trained using biophysical computational models that integrated electrostatics, bioheat transfer, and cell necrosis, along with magnetic resonance (MR) images of breast cancer patients. The computational model was validated through experiments using *ex vivo* bovine liver tissue. Our model demonstrated a Dice score of 96.3% in predicting lesion volume and a root mean squared error (RMSE) of 0.5624 for temperature distribution when tested with foreseen tumor images. Notably, even with unforeseen images, it achieved a Dice score of 93.8% for the ablation lesion and an RMSE of 0.7078 for the temperature distribution. All networks were capable of inferring results within 10 ms. The proposed technique, applied to optimize the placement of the electrode for a specific target region, holds significant promise for enhancing the safety and efficacy of RFA.

1. Introduction

Radiofrequency ablation (RFA) is a pivotal technique in the field of interventional medicine because of its ability to treat various medical conditions, particularly tumors, with minimal invasiveness (McDermott and Gervais, 2013; Abd El-Kader et al., 2018; Besler et al., 2020a). RFA uses the heat generated from electrical currents delivered through percutaneously inserted electrodes to induce coagulative necrosis in pathological tissues (Peek and Douek, 2017). Its significance lies in its effectiveness in eradicating a tumor while preserving healthy surrounding tissues, thus offering advantages over traditional surgical resection such as quick recovery, high efficacy, low complication rates, and cost-effectiveness (Lim, 2000; Zhu et al., 2013; Berjano, 2006).

Although surgical resection is the preferred treatment for eligible patients owing to its potential for complete tumor removal, RFA serves as an effective alternative for those who are unsuitable candidates for

resection. This may include patients with comorbidities, advanced age, or tumors located in areas that make surgical intervention risky. RFA is a minimally invasive option that can effectively target and destroy tumor cells, providing a valuable treatment option for individuals who cannot undergo surgery (Lanuti et al., 2009; Yi et al., 2014).

To achieve precise treatment, interventional radiologists adjust the clinical settings, such as the applied power, current duration, and insertion trajectory of the electrodes (Ho and Min, 2018; Widmann et al., 2009). However, quantitatively predicting the extent of ablation remains a challenging task, as treatment outcomes are influenced not only by device settings, but also by individual-specific characteristics and the surgeon's expertise. In general planning procedures, the ablation shapes are commonly assumed to be ellipsoids, based on manufacturer-provided ablation size guidelines designed primarily for homogeneous tissue. This approach overlooks the patient-specific factors that are

* Corresponding author.

E-mail address: yoonekh@yonsei.ac.kr (K. Yoon).<https://doi.org/10.1016/j.engappai.2024.109349>

Received 10 March 2024; Received in revised form 18 August 2024; Accepted 14 September 2024

Available online 26 September 2024

0952-1976/© 2024 The Author(s). Published by Elsevier Ltd. This is an open access article under the CC BY license (<http://creativecommons.org/licenses/by/4.0/>).

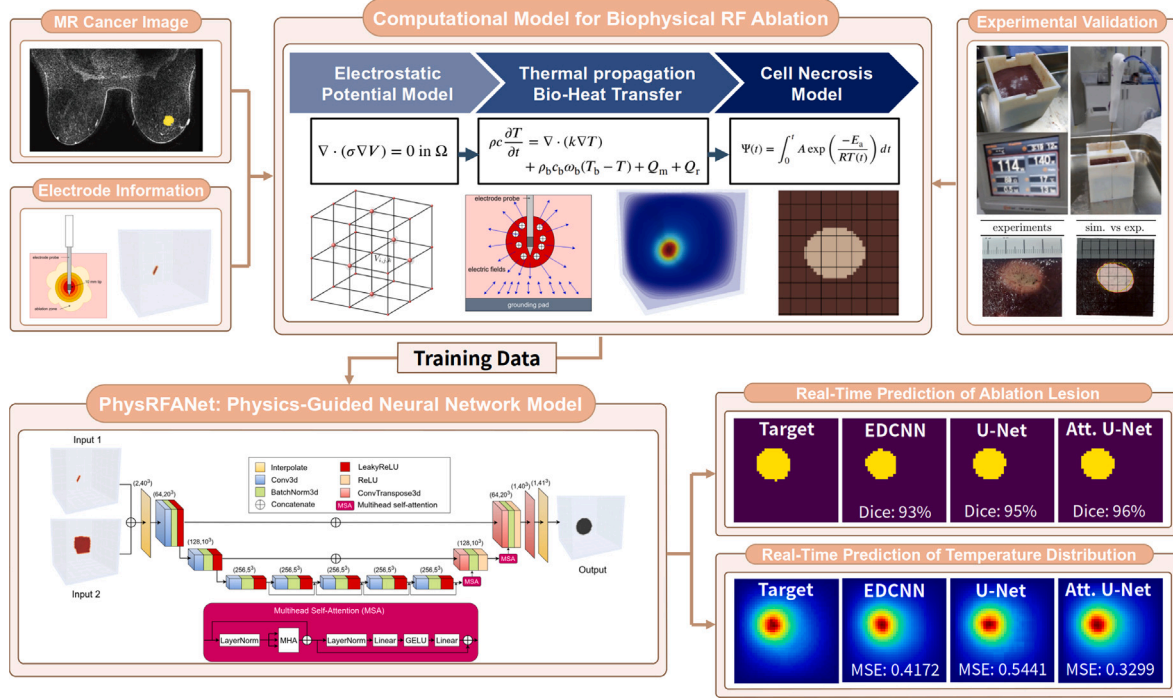


Fig. 1. Overall flowchart of real-time prediction method of thermal effect during radiofrequency ablation treatment.

crucial for achieving personalized and precise RFA treatment (Jiang et al., 2010; McCreedy et al., 2006).

Theoretical models and computer simulations serve as crucial tools for predicting the ablated region and improving therapeutic outcomes for individual patients by providing vital information on the electrical and thermal behaviors during RFA procedures (Berjano, 2006). The temperature distribution and the corresponding ablation lesions were obtained through the analysis of multi-biophysics models, which represent electrical conduction, bioheat transfer, and cell necrosis processes (Kröger et al., 2006; Shahidi and Savard, 1994; Singh and Repaka, 2018). However, achieving accurate predictions incurs significant computational cost, thereby imposing constraints on their practical application in clinical settings (Voglreiter et al., 2018).

Several efforts have been made to enhance the simulation speed for the intraoperative utilization of computational methods during RFA (Mariappan et al., 2017; Kath et al., 2019; Hoffer et al., 2022). These studies achieved significant reductions in computation time owing to the use of massively parallel computing on graphics processing units (GPU). However, even with these advancements, simulation times still range from a few seconds to minutes, depending on the size of the simulation domain. Furthermore, prolonged simulation times are necessary when utilizing more sophisticated models, such as coupled multiphysics analysis (Akbari and Giannacopoulos, 2021), and when considering the phase change effect of biological tissue (Abraham and Sparrow, 2007).

Recently, there has been an emerging trend to leverage deep learning algorithms for the efficient representation of complex physical phenomena that pose challenges for characterization through traditional mathematical analysis (Lutter et al., 2019; Mendizabal et al., 2020; Choi et al., 2022; Shin et al., 2023; Salehi and Giannacopoulos, 2022; Koh et al., 2022; Shin et al., 2024; Park et al., 2023). Within the domain of RFA treatment, a noteworthy study by Besler et al. (2020b) exemplified the potential of implementing real-time estimation of RFA lesion depth using a machine learning model combined with a statistical merging approach. The proposed system utilized multi-frequency impedance measurement data, achieving accuracy at the millimeter resolution. However, it is limited to providing only one-dimensional depth information of RFA lesions in a simple tissue representation

model. For the practical efficacy of such deep learning models in clinical settings, it is essential to accurately represent the multiphysics phenomena arising from the intricate morphologies of lesions.

In this paper, we present PhysRFANet, a set of deep neural networks designed to learn from computational simulations that capture the multiphysics phenomena inherent in RFA. Training data were generated through computational simulations of electrostatic, bioheat transfer, and cell necrosis models using magnetic resonance (MR) images obtained from 11 patients with breast cancer. The accuracy of the computational model was validated experimentally using *ex vivo* bovine liver tissues. We developed six network models based on three different architectures, each serving two specific purposes: to predict the temperature distribution and corresponding ablation lesion. The performance of these network models was evaluated using various metrics. To evaluate the robustness and generality of our model, we conducted further assessments using two new sets of patient data that were entirely excluded from the training process. A flowchart of the study process is shown in Fig. 1. The significance of the proposed model is summarized as follows.

- Computational biophysical models reflect the geometric characteristics of an individual patient's tumor using magnetic resonance (MR) imaging.
- Prediction accuracy of the computational model was validated using *ex vivo* bovine liver tissue.
- Neural network models were trained on the results of the computational model.
- Real-time personalized predictions of the thermal distribution and cell necrosis regions are available, given the tumor geometry and electrode placement.

2. Computational model

In this section, we describe the formulation of our computational model, which includes a geometric representation of the tumor tissue, electrical field calculation, bioheat transfer algorithm, and cell necrosis model.

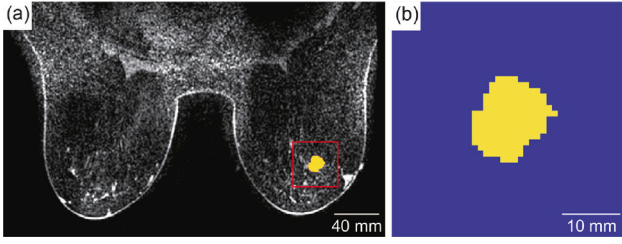


Fig. 2. An example of tumor geometric modeling from an MR image. (a) Overlay of tumor segmentation result (yellow region) onto the corresponding axial view MR image. The red box shows the boundary of the cropped FOV, and (b) shows the segmentation image in the FOV. The yellow region represents the tumor area, whereas the blue region represents normal tissue.

2.1. Tumor geometric model via MR image

MR images of 13 breast cancer patients from a publicly available dataset (Saha et al., 2018) were used to model the tumor geometry. The datasets consisted of dynamic contrast enhanced (DCE) MR images and the corresponding segmentation images, which were annotated by radiologists to depict the cancerous regions for each patient. All images were resampled to isotropic voxels of $1.0 \times 1.0 \times 1.0 \text{ mm}^3$ using the Lanczos filter algorithm (Burger and Burge, 2009). For computational efficiency, the simulation domain for each patient was defined by cropping it to a field of view (FOV) centered at the volumetric center of the tumor region with a size of $40 \times 40 \times 40 \text{ mm}^3$. The FOV size was sufficient to encompass the entire volume of the segmented tumor ($3021 \pm 2789 \text{ mm}^3$, $N = 13$). A visual representation of the geometric model of the tumor using MR images is shown in Fig. 2.

Employing segmented binary data from MR image data helps to avoid overfitting. Segmented tumor data can help avoid overfitting compared to the original MR image data for several reasons. First, it provides a focused view by isolating the region of interest, reducing the complexity of the input data, and removing irrelevant details. This allows the model to learn features specific to tumor detection and classification. Additionally, segmented data has lower dimensionality, which is easier to generalize from and reduces the risk of overfitting due to the “curse of dimensionality”. By focusing on the tumor region, the signal-to-noise ratio is enhanced, minimizing the likelihood of the model picking up noise and learning spurious patterns that do not generalize well to the new data. Segmented tumor data also benefit from clearer and more consistent annotations because the tumor is explicitly segmented, making it easier for models to learn from accurately annotated data.

2.2. Temperature-dependent electro-static analysis for electrical field

The quasi-static version of Maxwell’s equation was used to compute the resistive heating during RFA. This is relevant because within the RFA frequency range of 450–550 kHz, the wavelength of the electric field is substantially larger than the size of the active electrode, as noted by Singh and Repaka (2017). Thus, the electric potential was determined by solving the generalized Laplace equation

$$\nabla \cdot (\sigma \nabla V) = 0 \text{ in } \Omega, \quad (1)$$

where σ is the electrical conductivity (S/m), V is the electric potential (V) with the following boundary conditions, and Ω is a volumetric domain for analysis (Schumann et al., 2011):

$$\begin{cases} V(\mathbf{x}) = V_p, & \mathbf{x} \in \Gamma_e, \\ \mathbf{n}(\mathbf{x}) \cdot \nabla V(\mathbf{x}) = 0, & \mathbf{x} \in \Gamma_s, \end{cases} \quad (2)$$

where V_p is the applied power (W), Γ_e is the boundary of the domain covered by the electrodes, and Γ_s is the exterior surface boundary of simulation space.

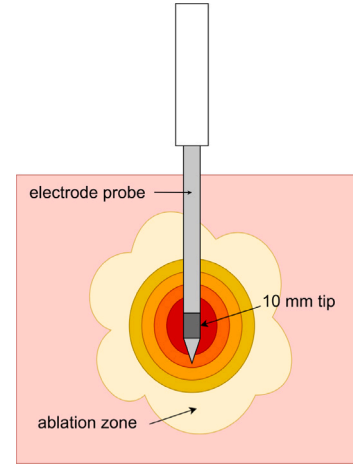


Fig. 3. The illustration represents a single-needle ablation electrode utilized for tumor ablation. A source voltage applied to the conductive tip facilitates the therapeutic intervention.

The finite element formulation of Eqs. (1) and (2) is expressed as follows:

$$\int_{\Omega} \sigma' \delta \mathbf{V}^T \left(\frac{\partial \mathbf{N}^T}{\partial x} \frac{\partial \mathbf{N}}{\partial x} + \frac{\partial \mathbf{N}^T}{\partial y} \frac{\partial \mathbf{N}}{\partial y} + \frac{\partial \mathbf{N}^T}{\partial z} \frac{\partial \mathbf{N}}{\partial z} \right) \mathbf{V} d\Omega = 0, \quad (3)$$

where \mathbf{V} is the discretized electrical potential at finite element nodes, \mathbf{N} is a linear interpolation matrix (i.e., $V = \mathbf{N}\mathbf{V}$), and δ indicates a variational symbol. Employing the standard finite element solution procedure with Eq. (3), the solution of electrical potential is obtained. The volumetric heat source due to resistive heating during RFA, denoted by Q_r (W/m³), is quantified by

$$Q_r = \sigma' |\nabla V|^2, \quad (4)$$

where the calculated Q_r is utilized as the heat input for the bioheat transfer analysis. It is known that the changes of the temperature-dependent electrical conductivity affect the outcome of the models (Chang, 2003; Watanabe et al., 2008; Trujillo and Berjano, 2013). The electrical conductivity σ' changes with temperature as follows:

$$\sigma' = \begin{cases} \sigma_{\text{normal}} (1 + 0.02 (T(t, \mathbf{x}) - T_0)), & T < 100 \text{ and } \mathbf{x} \in \Omega_{\text{normal}}, \\ 0.0001 \sigma_{\text{normal}}, & T \geq 100 \text{ and } \mathbf{x} \in \Omega_{\text{normal}}, \\ \sigma_{\text{tumor}} (1 + 0.02 (T(t, \mathbf{x}) - T_0)), & T < 100 \text{ and } \mathbf{x} \in \Omega_{\text{tumor}}, \\ 0.0001 \sigma_{\text{tumor}}, & T \geq 100 \text{ and } \mathbf{x} \in \Omega_{\text{tumor}}, \end{cases} \quad (5)$$

where subscripts “normal” and “tumor” represent normal tissue and tumor tissue, respectively.

Finite element models were constructed based on the tumor geometry described in Section 2.1. The electrical conductivity constant of the tumor tissue, σ_{tumor} , was set to 4 S/m, whereas that of the normal tissue, σ_{normal} , was set to 0.4 S/m (Zhao et al., 2013). The input voltage generated by an electrode tip with a length of 10 mm and a diameter of 1 mm was modeled by applying boundary conditions in Eq. (2) to all nodes encompassed by the electrode. Located at the end of the needle, the electrode tip releases high-frequency alternating current into the surrounding tissue, generating heat through radiofrequency energy. An illustration of a single-needle ablation electrode is presented in Fig. 3.

2.3. Bioheat transfer analysis for heat propagation

The Pennes bioheat model (Pennes, 1948) was used to model the bioheat transfer inside the breast tissue during RFA using the temperature-dependent resistive heat generation term:

$$\rho c \frac{\partial T}{\partial t} = \nabla \cdot (\kappa \nabla T) + \rho_b c_b \omega_b (T_b - T) + Q_m + Q_r, \quad (6)$$

where ρ is the density of tissue (kg/m³), c is the specific heat capacity of tissue (J/kg/K), T is temperature (°C), t is ablation time, κ is thermal conductivity of tissue (W/m/K), ρ_b is the density of blood, c_b is the specific heat of blood, ω_b is the perfusion rate of blood, T_b is the temperature of blood (37 °C), Q_m is metabolic heat generation (W/m³), and Q_r^t is temperature-dependent resistive heat generation (W/m³) obtained from Eqs. (4) and (5).

To solve Eq. (6), the finite-difference time-domain (FDTD) scheme was used (Berjano, 2006; Labonte, 1994; Kim et al., 2023),

$$\begin{aligned} \frac{\rho_{i,j,k} c_{i,j,k}}{\Delta t} (T_{i,j,k}^{t+\Delta t} - T_{i,j,k}^t) &= \frac{\kappa_{i,j,k}}{\Delta s^2} \left[(T_{i+1,j,k}^t - T_{i,j,k}^t) - (T_{i,j,k}^t - T_{i-1,j,k}^t) \right] \\ &+ \frac{\kappa_{i,j,k}}{\Delta s^2} \left[(T_{i,j+1,k}^t - T_{i,j,k}^t) - (T_{i,j,k}^t - T_{i,j-1,k}^t) \right] \\ &+ \frac{\kappa_{i,j,k}}{\Delta s^2} \left[(T_{i,j,k+1}^t - T_{i,j,k}^t) - (T_{i,j,k}^t - T_{i,j,k-1}^t) \right] \\ &+ \rho_b c_b \omega_b (T_b - T_{i,j,k}^t) + Q_{m,i,j,k} + Q_{r,i,j,k}^t, \end{aligned} \quad (7)$$

where Δt is the discretized time interval, $\rho_{i,j,k}$, $c_{i,j,k}$, $T_{i,j,k}$, $\kappa_{i,j,k}$, $Q_{m,i,j,k}$, and $Q_{r,i,j,k}^t$ are respectively the density, specific heat capacity, temperature, thermal conductivity, metabolic heat generation, and temperature-dependent resistive heat generation of tissue at the grid index i, j, k of the simulation domain, and Δs is the spatial discretization interval (i.e., grid interval).

Based on the segmented MR image in Section 2.1, thermal properties of the tumor tissue (density of 1050 kg/m³, specific heat capacity of 3770 J/kg/K, thermal conductivity of 0.48 W/m/K), normal tissue (density of 911 kg/m³, specific heat capacity of 2348 J/kg/K, thermal conductivity of 0.21 W/m/K), blood perfusion (blood density of 1050 kg/m³, blood specific heat capacity of 3617 J/kg/K, blood perfusion rate of 5.3 s⁻¹ for tumor tissue, blood perfusion rate of 0.2 s⁻¹ for normal tissue), and metabolic heat (400 W/m³ for normal tissue and 13,600 W/m³ for tumor tissue) were assigned to the simulation (Singh and Repaka, 2018). The initial temperatures of the tissues and blood were set to 37 °C. The simulations were conducted by applying the temperature-dependent resistive heat (i.e., $Q_{r,i,j,k}^t$) for 180 s with a time resolution (i.e., Δt) of 0.1 s and calculating the temperature distribution of the entire spatial domain at each time interval.

2.4. Cell necrosis model

The thermal damage of biological tissue (Ψ) is quantified using the first-order Arrhenius rate equation as follows (Singh and Repaka, 2018):

$$\Psi(t) = \int_0^t A \exp\left(\frac{-E_a}{RT(t)}\right) dt, \quad (8)$$

where A is the frequency factor ($= 1.18 \times 10^{44}$), E_a is the activation energy for irreversible damage reaction ($= 3.02 \times 10^5$ J/mol), R is the universal gas constant ($= 8.3134$ J/mol/K), T is the temperature (K) of the corresponding tissue.

The temperature distribution for each time step obtained in Section 2.3 was utilized to evaluate the cumulative tissue damage values of $\Psi(t)$ for every voxel. To delineate irreversible thermal damage, we applied a threshold of $\Psi(t) > 1$, classifying values exceeding this threshold as the damaged tissue region and values below it as the viable tissue region (Henriques, 1947).

2.5. Experimental validation

In this section, we describe the experimental setup for RFA designed to validate the accuracy and reliability of our RFA computational model. Freshly excised bovine liver procured from a local butcher shop on the day of the experiment was used as the experimental tissue. Seven cuboidal samples, each measuring approximately 10 × 10 × 10

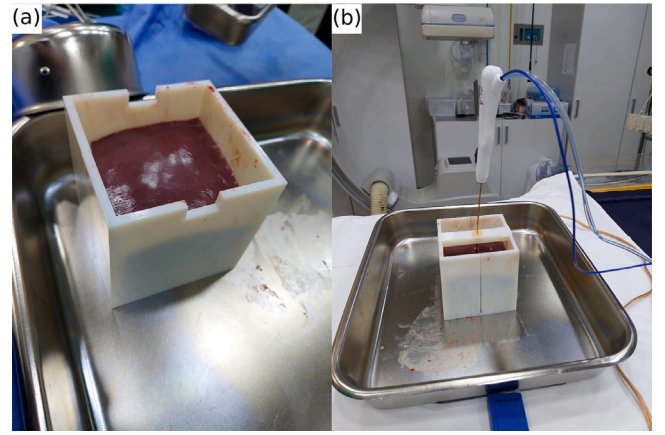


Fig. 4. Experimental setup for ex vivo tissue RFA. (a) A bovine liver sample is cut into a cuboidal shape and carefully placed within a 3D-printed container, (b) enabling accurate ablation at its center.

cm³, were prepared by cutting the bovine liver to fit within a custom-designed 3D-printed container, as shown in Fig. 4(a). This container was designed to facilitate precise RF ablation at the center of the liver sample, followed by halving the sample at the same location, as illustrated in Fig. 4(b).

A 17-gauge monopolar electrode with a tip length of 10 mm (V-tip; RF Medical, Seoul, Korea) was inserted at a depth of approximately 5 cm and positioned at the center of the liver sample. Radiofrequency waves were emitted from the electrode tip into the surrounding tissue for 3 min using a 200 W generator (M-3004; RF Medical, Seoul, Korea). After completing the ablation, the electrode was removed, and the bovine liver sample was bisected to obtain cross-sectional plane images. Distinct areas of coagulative necrosis were revealed in these images, identified and segmented using the “Segment Anything in Medical Images” code (Ma et al., 2023) for subsequent quantitative analysis.

The proposed computational model was validated using experimental results. A homogeneous tissue space with a resolution of 1 mm, spanning 40 × 40 × 40 mm³, was utilized, with an electrode placed at the central location of the simulation space. The initial electrical conductivity of the bovine liver tissue was set to 0.69 S/m (Fuentes et al., 2010). The thermal properties of the tissue included a density of 1079 kg/m³, a specific heat capacity of 3415.0 J/kg/K, and a thermal conductivity of 0.5 W/m/K (Silva et al., 2020); blood perfusion and metabolic heat terms were disregarded. The heat generated by radiofrequency energy was applied over a total duration of 180 s, using a time step of 0.1 s, starting from an initial temperature of 20 °C.

3. Neural network models

In this section, we employ three network models with different architectures for performance comparison. Specifically, for the purpose of basic performance benchmarking, the encoder-decoder based CNN (EDCNN) architecture was employed. The U-Net architecture with its symmetric encoder-decoder structure complemented by skip connections was the primary focus of this study. This design is known for its use of skip connections that combine deep coarse-grained feature maps from the decoder and shallow fine-grained feature maps from the encoder, effectively enhancing the target details (He et al., 2016; Huang et al., 2017; Hariharan et al., 2015; Lin et al., 2017).

Our objective is to develop lightweight neural network models that can perform predictions in real time. This involves optimizing the model architecture to be both efficient and responsive, ensuring that it can handle tasks quickly enough to meet the demands of real-time applications. By focusing on reducing computational complexity and memory usage, we aim to create a model that not only delivers

Table 1

Splitting of foreseen and unforeseen test datasets. The acronym “BT” represents the breast tumor dataset.

Training dataset	Test dataset
5000 (BT1-BT11)	Foreseen: 500 (BT1-BT11) Unforeseen: 500 (BT12-BT13)

accurate predictions but also does so with the speed necessary for real-time processing. Compared to networks like GANs (Goodfellow et al., 2014), diffusion models (Ho et al., 2020), and transformers (Vaswani et al., 2017; Liu et al., 2021), architectures such as EDCNN, U-Net, and Attention U-Net are significantly less computationally intensive and require fewer parameters, making them cheaper in terms of both memory usage and processing power.

3.1. Training and test data generation

The datasets used to train and test the network model were derived from the computational model described in Section 2. To ensure a diverse dataset, we conducted RFA simulations for each breast tumor MR image, utilizing 500 randomly placed electrode tip locations and directions within the tumor regions. Segmented breast tumor images (size of $41 \times 41 \times 41$) along with binary images (size of $41 \times 41 \times 41$) representing the placement of the electrode tip were utilized as network inputs, and either the corresponding coagulative tissue necrosis zones (size of $41 \times 41 \times 41$) or temperature distributions (size of $41 \times 41 \times 41$) obtained from the RFA simulation were respectively employed for the network output.

For the training datasets, we collected 5500 RFA simulation results derived from 11 distinct breast tumor images (BT1-BT11) of different patients. These data were then randomly split into 5000 samples for training and 500 samples for testing. Out of the 5000 training data samples, 200 were allocated to the validation set for hyperparameter tuning. In contrast, to evaluate the network’s performance on unseen MR images of breast tumors from a practical perspective, we utilized 500 RFA simulation results sourced from two distinct tumors (BT12 and BT13), each from a separate patient, as another test dataset. For better understanding, please refer to Table 1.

In the training of PhysRFANet, we carefully selected various hyperparameters to optimize the performance. To configure the optimization strategy of our model, we selected the Adam optimizer, initialized it at a learning rate of 0.001, and set the batch size to 16 for efficient processing. For the hyperparameter tuning during training, we implemented the “ReduceOnPlateau” learning rate scheduler. The scheduler was configured to reduce the learning rate by a factor of 0.5 if no improvement was observed in the valid loss over the five epochs. This approach allows for dynamic adjustment of the learning rate based on the performance of the model. The training was conducted for 100 epochs, utilizing “EarlyStopping” with a patience parameter of 10 to prevent overfitting and restore the model weights to those with the best validation performance. All training was performed on a single GPU, which utilized its parallel processing capabilities to expedite the training process.

3.2. Network architectures for the coagulative necrosis

In this section, we provide a thorough overview of the PhysRFANet architectures, showcasing them using visual diagrams complemented by in-depth explanations. A visual explanation of this is shown in Fig. 5. Each component and layer is detailed, emphasizing their specific roles and contributions to the overall system, as evidenced by ablation studies.

The EDCNN model shown in Fig. 5(a) is a CNN specifically tailored for 3D data. It consists of an encoder and decoder, which are a series of 3D convolutional layers, each followed by batch normalization and

ReLU activation, designed to extract and compress features from the input. The encoder uses strides to reduce the spatial dimensions, similar to downsampling. The decoder, aimed at reconstructing the data to a higher resolution, employs transposed 3D convolutional layers accompanied by batch normalization and ReLU activations. In the forward pass, the model concatenates two types of input data, indicating its capability to handle dual input modalities, a common scenario in medical imaging tasks. The final layers reduce the channel dimensions to one to match the size of the input. In addition, the model adopts specific weight initialization strategies for its layers, indicating a focus on efficient training convergence.

The U-Net architecture shown in Fig. 5(b) includes encoder, mid-layers, and decoder classes. The encoder performs downsampling and mid-layers processing of features at the network bottleneck, while the decoder handles the upsampling. These modules use convolutional layers, batch normalization, and activation functions suitable for processing 3D data. The U-Net architecture concatenates and processes inputs through the downscaling, middle, and upscaling modules. The architecture is designed for tasks that involve volumetric data.

The Attention U-Net model shown in Fig. 5(c) is a sophisticated neural network architecture that blends a U-Net structure with self-attention mechanisms. This design is especially suitable for complex applications, such as medical image analysis, which require both local and global contextual understanding. The network features self-attention modules that implement multi-head attention to capture long-range dependencies within the data, accompanied by layer normalization and feedforward networks for further refinement. The architecture is structured along a U-Net framework, with the encoder constituting the downsampling path. These modules employ 3D convolutions, batch normalization, and LeakyReLU activation to incrementally extract complex features while reducing the spatial dimensions. The middle layers process these features using skip connections for added efficiency. The upsampling path, which is composed of a decoder, increases the spatial dimensions and integrates features from the downsampling path, thereby enhancing detail retention. Self-attention modules are interspersed in the upsampling path, augmenting the network’s focus on salient features. The forward method defines the workflow starting with the concatenation of two input data types and proceeding through the successive network layers with optional interpolation of the input and output to specific dimensions.

3.3. Network architectures for the temperature distribution

The same network architectures described in Section 3.2 are utilized for analyzing the temperature distribution. The primary distinction between the networks shown in Figs. 5(a) and 6 lies in their outputs. As in the previous section, ablation studies are conducted to determine how network performance is affected by changes in various components.

3.4. Loss function

For network training of the ablated lesion zone, we employed the Dice loss function, which is defined as follows:

$$\mathcal{L}_{\text{Dmg}}(x, \tilde{x}) = \text{Dice}(x, \tilde{x}) = 1 - \frac{2 \sum_{i=1}^n x_i \tilde{x}_i}{\sum_{i=1}^n x_i^2 + \sum_{i=1}^n \tilde{x}_i^2}, \quad (9)$$

where \tilde{x}_i and x_i represent the components at the i th position in the ground truth and the corresponding ablation lesion prediction, respectively.

For network training of the temperature distribution, we utilized a loss function that combined the mean squared error (MSE), weighted MSE, and Dice_(>50) loss. To introduce a weighted MSE loss function, define a mask m as follows:

$$m_i = \begin{cases} 1, & \text{if } x_i > 50^\circ\text{C}, \\ 0, & \text{otherwise.} \end{cases} \quad (10)$$

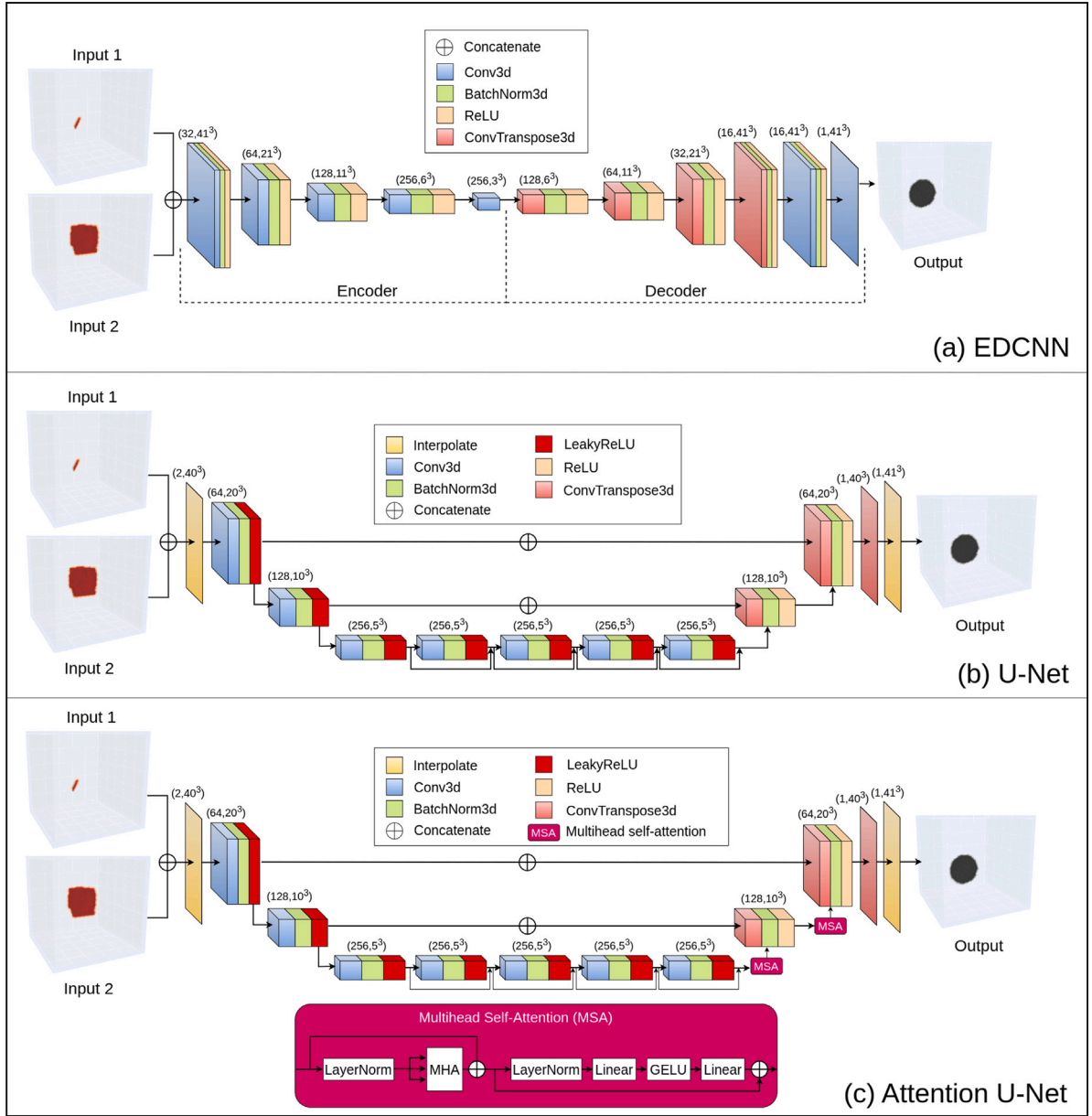


Fig. 5. Three network architectures: (a) EDCNN, (b) U-Net, and (c) Multihead-Self-Attention U-Net architectures. The input 1 is the geometry of the electrode tip and the input 2 is the segmented breast tumor from the MR image. The output is the predicted ablation lesion zone. For all RFA lesion zone network training, the Dice loss function is used.

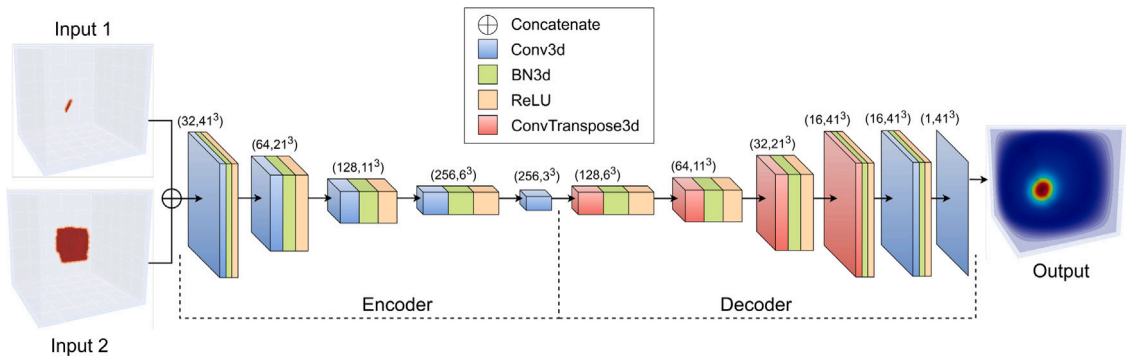


Fig. 6. EDCNN architecture, where Input 1 comprises the electrode tip geometry and Input 2 is the segmented breast tumor from the MR image. The output is the predicted temperature distribution map. The U-Net and Attention U-Net architectures employed for temperature distribution prediction are identical to those in Fig. 5(b) and (c), with the primary difference being the output, which is now the temperature distribution. The combined loss function Eq. (13) with $(\alpha, \beta, \gamma) = (0.7, 0.0, 0.3)$ is used for all network training for the temperature distribution.

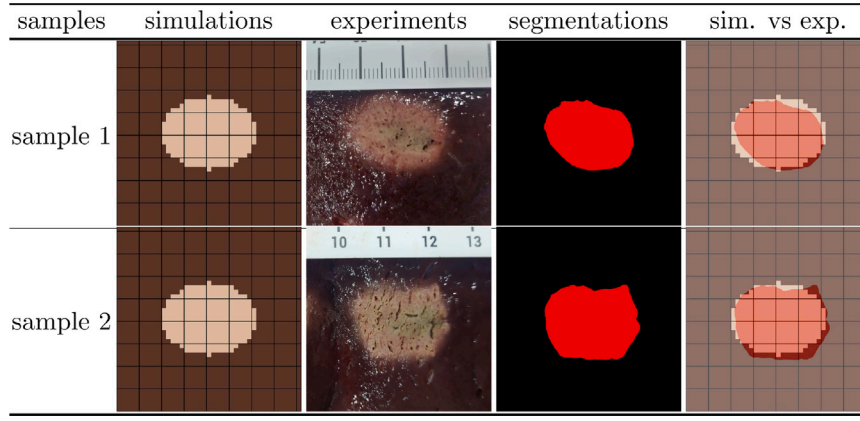


Fig. 7. Comparison of simulated coagulative necrosis and RFA experiment results for two homogeneous liver tissue samples. The real electrode tip is positioned at the center of the bovine liver placed in a cubic box, and similarly, the electrode tip in the numerical simulation is located at the center of the computational domain. This alignment ensures that the actual necrotic region closely matches the simulation results. The leftmost figures illustrate the numerical simulation outcomes. The second column represents experimental results. The third column shows segmented necrotic regions (red) obtained using MedSAM (Ma et al., 2023). The last column displays the segmented coagulative necrotic regions (red) with overlaid simulated results. Naturally, the deterministic numerical simulation results remain the same under identical conditions; however, the experimental necrotic regions demonstrate slight variations.

where \tilde{x}_i and x_i denote the elements at the i th position in the ground truth and the corresponding temperature distribution prediction, respectively. We implemented the weighted MSE loss function that applies the weight ω to the MSE loss for elements where the mask is 1 (above the threshold). The MSE loss remains unchanged where the mask is 0, enabling accurate prediction of the temperature distribution in the region of interest with elevated temperatures exceeding 50 °C. The weighted MSE loss function is defined as

$$\mathcal{L}_1(x, \tilde{x}) = \frac{1}{n} \sum_{i=1}^n (x_i - \tilde{x}_i)^2 (\omega m_i + (1 - m_i)). \quad (11)$$

The Dice_(>50) loss function is defined as

$$\text{Dice}_{(>50)}(x, \tilde{x}) = 1 - \frac{2 \sum_{i=1}^n x_i (>50) \tilde{x}_i (>50)}{\sum_{i=1}^n x_i^2 (>50) + \sum_{i=1}^n \tilde{x}_i^2 (>50)}. \quad (12)$$

In particular, the Dice_(>50) loss function relies on the temperature (50 °C) at which the cell death pattern transitions to a predominance of necrosis, as discussed in Zhang et al. (2018). The combined loss function is as shown below:

$$\mathcal{L}_{\text{Temp}}(x, \tilde{x}) = \frac{\alpha}{n} \sum_{i=1}^n (x_i - \tilde{x}_i)^2 + \beta \mathcal{L}_1(x, \tilde{x}) + \gamma \text{Dice}_{(>50)}(x, \tilde{x}), \quad (13)$$

where x and \tilde{x} are predictions and ground truth, respectively, and α , β , and γ are weights.

4. Results

In this section, we present the evaluation metrics employed, experimental validation, evaluation of the prediction accuracy, and inference time of the proposed network models. To demonstrate the robustness of the developed network, a validation was conducted using unforeseen tumor image data obtained from a new patient.

4.1. Evaluation metrics

All the evaluation metrics represent the differences between the predicted and simulated temperatures. The root mean squared error (RMSE), mean absolute error (MAE), and Dice score were used to evaluate the test outcomes for the temperature distribution. Specifically, the Dice scores, represented as Dice_(>40) and Dice_(>50), correspond to the temperature maps exceeding 40 °C and 50 °C, respectively. In addition, Dice score (Sorenson, 1948; Dice, 1945), Jaccard score (Jaccard, 1912), and Hausdorff distance (Rockafellar and Wets, 1998) are used to

evaluate test outcomes of the ablation lesions. The Hausdorff distance $d_H(X, Y)$ between two sets X and Y is defined as follows:

$$d_H(X, Y) = \max \left\{ \max_{x \in X} d(x, Y), \max_{y \in Y} d(X, y) \right\}, \quad (14)$$

where $d(a, B) = \min_{b \in B} d(a, b)$.

4.2. Experimental validation

In this section, we compare the outcomes of the RFA simulations with the RFA experimental results to validate the accuracy of the numerical RFA simulation. Because the bovine livers used in this *ex vivo* experiment did not include tumors, we did not incorporate tumors in the numerical simulation. Our primary objective was to demonstrate that in a homogeneous liver tissue, the numerical simulation accurately represents the real necrotic regions under the same conditions. This explains why the numerical simulation results for Samples 1 and 2 in Fig. 7 are identical. Although we were unable to include real tumor tissue in this experiment, we showed the similarity between the numerical results and experimental outcomes in a homogeneous environment. Except for the *ex vivo* experiment described in Section 4.2, all other numerical simulations included tumor tissues. Fig. 7 presents a comparative analysis of two exemplary samples, selected from a total of seven samples, demonstrating the simulated coagulative necrosis alongside the results of the RFA experiments.

Table 2 shows the length measurements, both horizontally and vertically, passing through the center of gravity of the necrotic region, along with its corresponding area. The center of gravity was determined using the `scipy.ndimage.center_of_mass` function (SciPy, 2023), and the horizontal and vertical lengths were obtained using the ImageJ software (Schneider et al., 2012). The results demonstrated an average accuracy within 3.28% for the aspect of the area. As shown in Table 2, we also included the t-test results to demonstrate that the experimental samples were sufficiently close to the simulation results. A p -value greater than 0.05 indicates that the simulation results are a good representation of the experimental samples.

4.3. Training and validation process

In this section, we examine the training and validation processes of the models used to predict the ablation lesions and temperature distribution. The loss curves depict how the training and validation losses of the model evolved over the training epochs. These graphs

Table 2

Comparison of RFA simulation outcomes and experimental segmentation data using various metrics. The term “samples” denotes the experimental sample numbers. “Horizontal” and “Vertical” refer to the lengths of lines in millimeters (mm), and ‘Area’ signifies the segmentation size in square millimeters (mm²). The “Difference” columns show the deviation of each sample from the simulation results. Descriptive statistics, differences, 95% confidence intervals (CI), and t-test results for each sample compared to simulation values are also provided. Including the *t*-statistic and *p*-value in the table allows for detailed statistical analysis, indicating whether there is a significant difference between the experimental samples and the simulation values. Since the *p*-value is greater than 0.05, this suggests no significant difference, indicating that the experimental samples are sufficiently close to the simulation results.

Sample	Horizontal (mm)		Vertical (mm)		Area (mm ²)	
	Value	Difference (%)	Value	Difference (%)	Value	Difference (%)
1	19.67	−1.33 (−6.33%)	15.87	−0.13 (−0.81%)	255.71	−9.29 (−3.51%)
2	20.51	−0.49 (−2.33%)	15.72	−0.28 (−1.75%)	304.93	+39.93 (+15.07%)
3	23.12	+2.12 (+10.10%)	14.03	−1.97 (−12.31%)	253.33	−11.67 (−4.40%)
4	17.72	−3.28 (−15.62%)	12.73	−3.27 (−20.44%)	212.15	−52.85 (−19.94%)
5	16.12	−4.88 (−23.24%)	15.73	−0.27 (−1.69%)	223.52	−41.48 (−15.65%)
6	21.84	+0.84 (+4.00%)	16.41	+0.41 (+2.56%)	307.29	+42.29 (+15.96%)
7	19.51	−1.49 (−7.10%)	16.69	+0.69 (+4.31%)	237.29	−27.71 (−10.46%)
avg ± sd	19.78 ± 2.37		15.31 ± 1.42		256.32 ± 37.33	
Simulation	21.00		16.00		265.00	
95% CI	[17.59, 21.97]		[14.00, 16.62]		[221.80, 290.84]	
<i>t</i> -statistic	−1.36		−1.28		−0.62	
<i>p</i> -value	0.223		0.246		0.561	

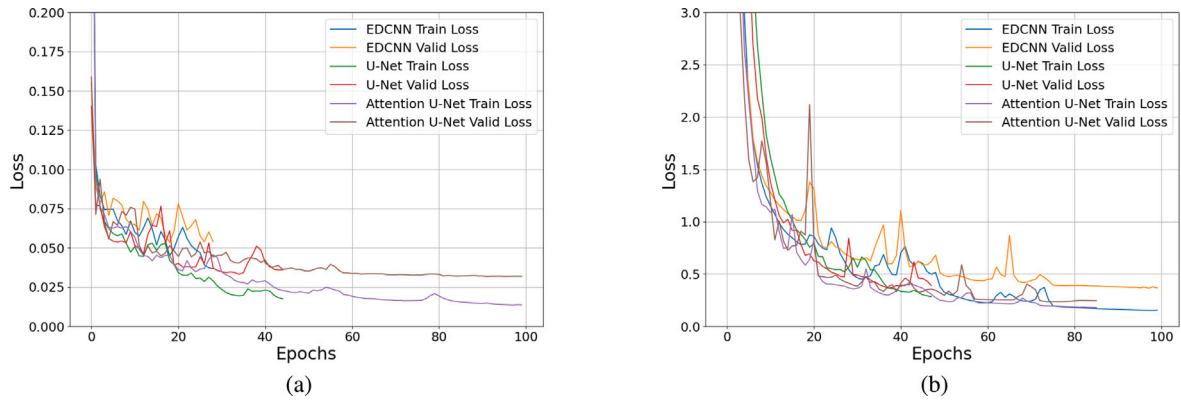


Fig. 8. Comparison of training and validation losses across different models. (a) displays the training and validation losses for ablation lesions, while (b) illustrates the training and validation losses for temperature distribution.

provide valuable insights into the learning dynamics of each model, including how quickly they converge, whether they overfit, and how well they are generalized to the validation data.

As shown in Fig. 8, both the U-Net and Attention U-Net demonstrated effective learning and strong generalization. In particular, Attention U-Net consistently outperformed across both tasks, exhibiting lower and more stable loss curves during both training and validation. This indicates that Attention U-Net is the most robust model and is highly capable of generalizing unseen data.

4.4. Evaluation of ablation lesion with foreseen/unforeseen test dataset

We presented an evaluation of the RFA lesion zone, demonstrating the performance of three different network architectures using both foreseen and unforeseen test datasets. Table 3 presents the prediction accuracy of the damaged volume for each network model under the conditions of the foreseen and unforeseen datasets. In the case of testing using a foreseen dataset, both the U-Net and Attention U-Net architectures demonstrated a higher predictive accuracy than the EDCNN. Specifically, U-Net and Attention U-Net exhibited nearly identical accuracies with a Dice score of 96.3%. However, the test using an unforeseen dataset showed a slightly lower accuracy than the foreseen dataset tests. However, when the Attention U-Net architecture was used, it achieved the highest Dice accuracy of 93.8% among the tested network models for the unforeseen dataset.

Table 3

Comparison of prediction accuracy for ablation lesion zone on foreseen/unforeseen test datasets.

Test sets	Networks	Dice	Jaccard	Hausdorff
Foreseen	EDCNN	0.9368	0.8844	1.3516
	U-Net	0.9555	0.9161	1.0844
	Att. U-Net	0.9633	0.9301	1.0632
Unforeseen	EDCNN	0.9116	0.8411	1.3489
	U-Net	0.9352	0.8801	1.2760
	Att. U-Net	0.9387	0.8860	1.1242

Fig. 9 shows an exemplar graphical comparison of the ablation lesion predictions with an unforeseen test dataset. An upward trend in accuracy was observed across the EDCNN, U-Net, and Attention U-Net, with each subsequent model exhibiting improved performance over its predecessor. Among the three models, the Attention U-Net exhibited the highest accuracy, indicating a progressive enhancement in the ability to analyze and interpret data correctly with each advanced model iteration.

4.5. Evaluation of temperature distribution with foreseen/unforeseen test dataset

Prior to assessing the performance of the presented network models in predicting temperature distribution, we conducted tests involving













methods	xy	yz	zx	Dice	Jaccard	Hausdorff
Target						
EDCNN				0.8398	0.7238	2.0000
U-Net				0.9512	0.9070	1.0000
Att. U-Net				0.9535	0.9112	1.0000

Fig. 9. Comparison of ablation lesion predictions from various networks on an unforeseen test dataset with the target (simulation result) for a single sample. A positive trend in accuracy is observed in the order of EDCNN, U-Net, and Attention U-Net.

Table 4

Comparing the performance of loss functions using different weight combinations on the foreseen and unforeseen test datasets for the temperature distribution. The U-Net is employed for this evaluation. The row highlighted in gray indicates the weight combination that delivers the best overall performance for both the foreseen and unforeseen test datasets. (num_epochs = 30).

(α, β, γ)	Foreseen					Unforeseen				
	MSE	RMSE	MAE	Dice _(>40)	Dice _(>50)	MSE	RMSE	MAE	Dice _(>40)	Dice _(>50)
(1.0, 0.0, 0.0)	0.5856	0.7459	0.4571	0.9695	0.9692	0.9246	0.9435	0.6059	0.9642	0.9523
(0.9, 0.1, 0.0)	0.6588	0.7911	0.4825	0.9704	0.9715	1.0160	0.9910	0.6394	0.9620	0.9467
(0.9, 0.0, 0.1)	0.6559	0.7891	0.4717	0.9673	0.9712	1.0198	0.9921	0.6357	0.9610	0.9460
(0.8, 0.2, 0.0)	0.9148	0.9324	0.5910	0.9758	0.9668	1.4023	1.1552	0.7471	0.9632	0.9391
(0.8, 0.1, 0.1)	0.6349	0.7764	0.4667	0.9663	0.9683	1.0795	1.0193	0.6501	0.9620	0.9486
(0.8, 0.0, 0.2)	0.6817	0.8043	0.4949	0.9714	0.9724	1.1685	1.0587	0.6809	0.9603	0.9457
(0.7, 0.3, 0.0)	0.7061	0.8183	0.4999	0.9694	0.9617	1.2274	1.0843	0.7104	0.9643	0.9328
(0.7, 0.2, 0.1)	0.7129	0.8276	0.5112	0.9531	0.9518	1.1441	1.0435	0.6590	0.9507	0.9358
(0.7, 0.1, 0.2)	0.9385	0.9461	0.6226	0.9775	0.9611	1.7180	1.2840	0.8643	0.9639	0.9247
(0.7, 0.0, 0.3)	0.5342	0.7124	0.4249	0.9668	0.9701	0.8934	0.9263	0.5857	0.9627	0.9539
(0.6, 0.4, 0.0)	0.6127	0.7634	0.4584	0.9671	0.9730	0.8944	0.9240	0.5816	0.9595	0.9534
(0.6, 0.3, 0.1)	0.5519	0.7266	0.4349	0.9627	0.9603	0.9615	0.9564	0.5979	0.9555	0.9452
(0.6, 0.2, 0.2)	0.6739	0.8032	0.4914	0.9574	0.9485	1.1725	1.0517	0.6624	0.9523	0.9251
(0.6, 0.1, 0.3)	0.6435	0.7864	0.4872	0.9738	0.9678	1.0209	0.9920	0.6378	0.9651	0.9482
(0.6, 0.0, 0.4)	0.8478	0.8947	0.5518	0.9734	0.9683	1.3125	1.1248	0.7259	0.9639	0.9389

different weight distributions (α, β, γ) for the combined loss function defined in Eq. (13). Table 4 indicates that $(\alpha, \beta, \gamma) = (0.7, 0.0, 0.3)$ yields one of the best metrics. The selection of weights $(0.7, 0.0, 0.3)$ is appropriate as minimizing the RMSE requires alpha to be the primary factor, dominating β and γ . The small values of beta and gamma allow for slight refinements, particularly enhancing the accuracy in critical high-temperature regions. Therefore, we adopted the determined weight distribution for the weighted loss function during the training process.

Table 5 presents the prediction accuracy of the temperature distribution for each network model under the conditions of the foreseen and unforeseen datasets. In the case of a test using the foreseen datasets, it was observed that Attention U-Net achieved the highest accuracy among the three network architectures, with an RMSE of 0.5624. In the case of unforeseen results, there was a slight decrease in the prediction accuracy compared with the foreseen test results. However, when the Attention U-Net architecture was used, a notable RMSE of 0.7078 was observed.

Table 5

Performance comparisons of temperature distribution on a foreseen/unforeseen test dataset.

Test sets	Networks	MSE	RMSE	MAE	Dice _(>40)	Dice _(>50)
Foreseen	EDCNN	0.4172	0.6199	0.3865	0.9594	0.9645
	U-Net	0.5441	0.7211	0.4497	0.9742	0.9775
	Att. U-Net	0.3299	0.5624	0.3595	0.9734	0.9795
Unforeseen	EDCNN	0.8261	0.8816	0.5507	0.9607	0.9503
	U-Net	0.9302	0.9465	0.6108	0.9677	0.9490
	Att. U-Net	0.5183	0.7078	0.4623	0.9707	0.9610

Fig. 10 presents an exemplar graphical comparison of the temperature distribution predictions with an unforeseen test dataset. All three network models exhibited results that closely resembled the target temperature distribution. Consistent with the results in Table 5, the Attention U-Net demonstrated the highest overall accuracy. Although the

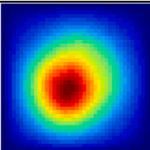
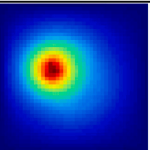
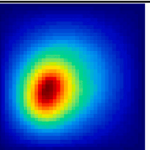
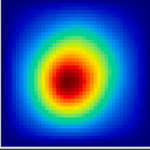
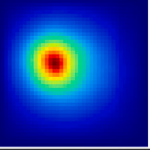
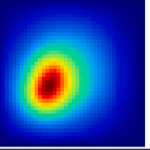
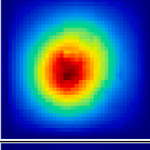
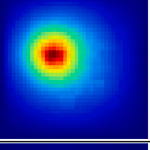
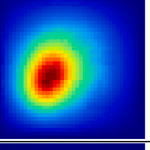
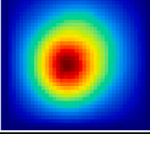
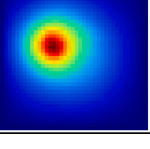
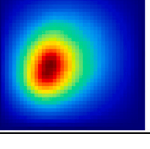
methods	xy	yz	zx	MSE	RMSE	MAE	Dice _(>40)	Dice _(>50)
Target								
EDCNN				0.6550	0.8093	0.4982	0.9769	0.9724
U-Net				0.6650	0.8155	0.5257	0.9818	0.9793
Att. U-Net				0.3321	0.5763	0.3860	0.9771	0.9790

Fig. 10. Comparison of temperature distribution predictions from various networks on an unforeseen test dataset with simulation results for a single sample.

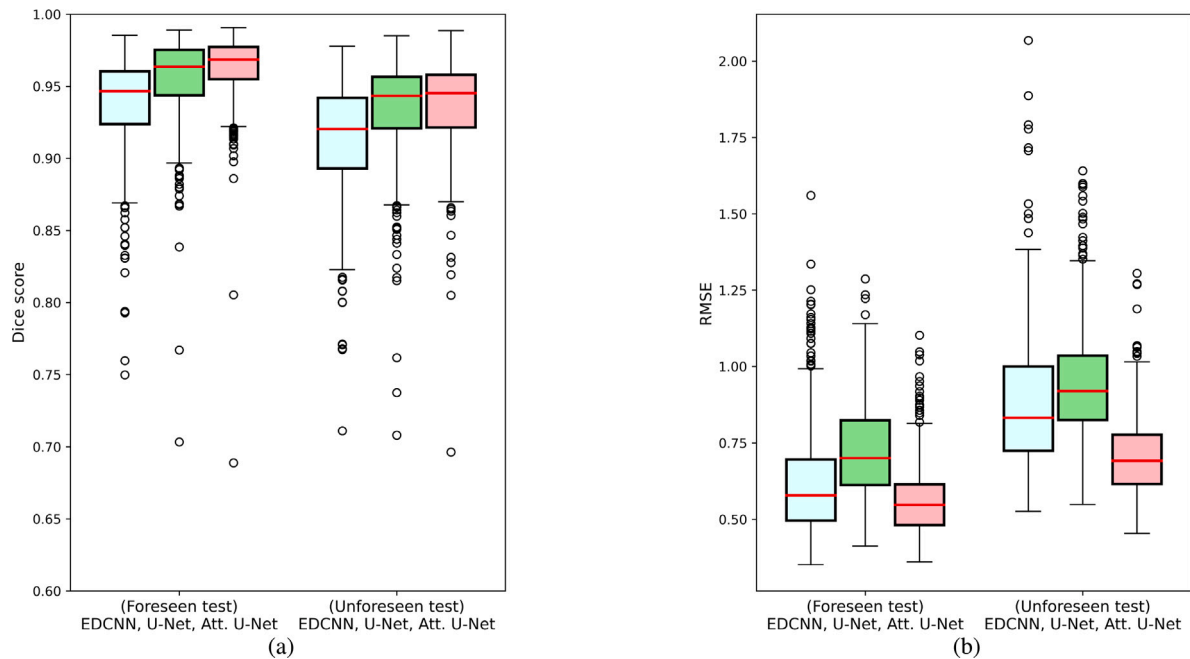


Fig. 11. Comparison of Dice score results and RMSE evaluations for different methods using both foreseen and unforeseen datasets. (a) represents the ablation lesion zone, while (b) corresponds to the temperature distribution. The three on the left were evaluated using a foreseen dataset, while the three on the right were assessed with an unforeseen dataset. The median value is denoted by the red horizontal line, while the interquartile range (IQR: from Q1 to Q3) is represented by the rectangle.

weighted Dice scores of U-Net and Attention U-Net were comparable, Attention U-Net showed lower RMSE and MAE.

Figs. 11(a) and 11(b) show the box plots of the ablation lesion volume and thermal distribution, respectively. In both cases, it is evident that the highest accuracy was achieved by Attention U-Net. U-Net is well-known for its excellent segmentation capabilities, which make it effective in predicting thermal ablation lesions; however, it does not perform as effectively in predicting the thermal distribution.

4.6. Evaluation of inference time

In this section, we compare the inference times across the three different network architectures to assess their suitability for real-time inferences. A significant decrease in time required to draw inferences is crucial for enabling precise, real-time prediction of incidents in both engineering and biomedical fields (Meng et al., 2024; Finkeldey et al., 2020; Liu et al., 2024; Wu et al., 2021). As listed in Table 6, the

Table 6
Comparisons of inference times across different network architectures.

Networks	Inference time (ms)
EDCNN	2.7579
U-Net	2.8312
Attention U-Net	3.6442

inference times for the EDCNN, U-Net, and Attention U-Net were approximately 2.7579, 2.8312, and 3.6442 ms, respectively. This implies that the prediction of thermal effects (i.e., ablation lesion zone and temperature distribution) during RFA treatment can be completed in less than 10 ms with two inputs: a segmented breast tumor MR image and the placement of the ablation tip setup. The inference time was measured using a parallel GPU computation on a desktop computer (AMD Ryzen 9 5950x 12-core processor 3.40 GHz and NVIDIA GeForce RTX 3090).

5. Discussion

Digital twin, which is a representation of real-world objects, processes, and systems in a virtual space, is at the forefront of the era of digital transformation. In the healthcare domain, it has the potential to precisely monitor treatment processes and analyze patient conditions, paving the way for personalized therapies and diagnostics. One crucial aspect in realizing this technology is the real-time simulation of the physical phenomena occurring in the target object. Recent efforts have integrated mathematical analysis models with artificial intelligence (AI) techniques, resulting in the creation of AI models capable of the real-time inference of physical phenomena. In this paper, we propose physics-guided network models that can provide users with real-time feedback information on the thermal effects that occur during RFA. The developed model achieved 96.3% accuracy in predicting the ablation lesion volume in terms of the Dice score and showed a temperature distribution difference of 0.5624 in terms of RMSE evaluation. Even in the evaluation using unforeseen data, the network demonstrated robust performance, with a 93.6% Dice score for ablation lesion prediction and an RMSE of 0.7078 for temperature prediction. Furthermore, all network models exhibited real-time capabilities, inferring thermal effects within 10 ms (over 100 frames per second) using only standard home desktop computer specifications.

To assess the robustness of the networks for new patients, we conducted an accuracy evaluation using unforeseen data not involved in training the network model. As presented in Tables 3 and 5, the results indicate a minor decline in performance compared to the results from the data previously seen during training. Nevertheless, the networks still achieved high accuracy levels, highlighting the generality of PhysRFANet and its capacity to adapt accurately to new breast tumor MR image data from new patients.

Although the use of *ex vivo* bovine liver tissue in the experiments validated our models, it is crucial to acknowledge its deficiency in replicating the dynamic physiological conditions inherent to living human patients (Kim et al., 2011). The differences between bovine and human organs, such as spatial relationships with other heat-sensitive organs, tissue cooling by neighboring blood vessels (Künzli et al., 2011), blood flow dynamics (Patterson et al., 1998), immune responses (Mauda-Havakuk et al., 2022), and other metabolic activities, may have affected the generalizability of our results to human clinical scenarios. Despite this limitation, the use of *ex vivo* bovine liver tissue offers a practical approach for preliminary investigations, laying the groundwork for further studies in more complex and clinically relevant settings.

It is also noteworthy that without the integration of detailed blood vessel information through high-resolution magnetic resonance angiography (MRA), predictions remain inaccurate because they rely on assumptions about blood flow that may not reflect actual physiological conditions. In this scenario, our modified Pennes bioheat model offers a

strong alternative to models that incorrectly account for heat loss owing to inaccurate blood flow assumptions, such as one-way flow.

This study did not consider RFA needle deflection or displacement (de Jong et al., 2018; Pérez et al., 2022) or deformation of the patient’s breast tissue (Danch-Wierzchowska et al., 2020) during RFA tip insertion. Neglecting these aspects could potentially affect the accuracy of the RFA procedure because tissue displacement resulting from changes in breast shape and needle deflection during tip insertion must be considered for precise treatment planning. Addressing these factors is a promising avenue for future research.

To effectively utilize the developed models in clinical practice, they must be integrated with a technique for the precise placement of RFA electrodes. For example, fusion imaging technology, specifically the integration of CT/MR-US fusion imaging, has significantly improved the accuracy of RFA (McWilliams et al., 2010; Makino et al., 2016; Wood et al., 2010; Kruecker et al., 2011). Integrated approach using PhysRFANet and fusion imaging technology can lead to more targeted and effective application of RFA, thereby minimizing procedural errors and optimizing therapeutic outcomes.

6. Conclusion

This study introduced a novel approach that leverages physics-guided network models to provide real-time feedback on thermal effects during RFA treatment. Using MR images from 13 breast cancer patients, our approach has successfully demonstrated its ability to simulate the multi-biophysics phenomena involved in RFA procedures. By incorporating temperature-dependent electrical conductivity, we have improved the realism of the simulations compared to the original Pennes bioheat model. Although the current model is primarily based on geometric differences in segmented tumors and does not incorporate other patient-specific *in vivo* measurements, such as thermal and electrical conductivity or tissue density, our workflow is designed to be adaptable for future integration with such measurements. As we continue to expand our research, future work will involve conducting various *in vivo* experiments to further refine the model, ensuring it accurately captures the complex and individualized biophysical interactions during RFA, ultimately supporting personalized treatment planning and optimization in clinical settings. Moreover, the proposed deep learning-based model holds great promise not only in advancing the standards of medical interventions and ensuring the safety and efficacy of RFA treatment, but also in broadening the scope of RFA applications.

CRedit authorship contribution statement

Minwoo Shin: Writing – original draft, Visualization, Validation, Software, Methodology, Data curation. **Minjee Seo:** Writing – review & editing, Data curation. **Seonaeng Cho:** Writing – review & editing, Data curation. **Juil Park:** Validation, Methodology. **Joon Ho Kwon:** Validation, Data curation. **Deukhee Lee:** Methodology. **Kyungho Yoon:** Writing – review & editing, Supervision, Methodology, Funding acquisition, Conceptualization.

Declaration of competing interest

The authors declare that they have no known competing financial interests or personal relationships that could have appeared to influence the work reported in this paper.

Data availability

The dataset, source code, and the description are available at <https://github.com/iangilan/PhysRFANet>.

Acknowledgments

The work was supported in part by the Korea Institute of Science and Technology (KIST) Institutional Program under Grant 2E31071, and in part by the National Research Foundation of Korea (NRF) grant funded by the Korean government (MSIT) (No. RS-2024-00335185).

References

- Abd El-Kader, A.M., Ali, H.E., Gad, M.A., Abdel Aziz, B.A., Hassanien, S.E.A., Hasaneen, A., Mitwally, R.A., 2018. Percutaneous radiofrequency ablation compared with surgical resection in the treatment of early hepatocellular carcinoma. *Egypt. J. Surg.* 37 (3), http://dx.doi.org/10.4103/ejs.ejs_97_17.
- Abraham, J., Sparrow, E., 2007. A thermal-ablation bioheat model including liquid-to-vapor phase change, pressure- and necrosis-dependent perfusion, and moisture-dependent properties. *Int. J. Heat Mass Transfer* 50 (13), 2537–2544. <http://dx.doi.org/10.1016/j.ijheatmasstransfer.2006.11.045>.
- Akbari, A., Giannacopoulos, D., 2021. An efficient multi-threaded Newton-Raphson algorithm for strong coupling modeling of multi-physics problems. *Comput. Phys. Comm.* 258, 107563. <http://dx.doi.org/10.1016/j.cpc.2020.107563>.
- Berjano, J., 2006. Theoretical modeling for radiofrequencyablation: state-of-the-art and challenges for the future. *Biomed. Eng. Online* 5 (1), 24. <http://dx.doi.org/10.1186/1475-925X-5-24>.
- Besler, E., Wang, Y.C., Sahakian, A.V., 2020a. Early and late fusion machine learning on multi-frequency electrical impedance data to improve radiofrequency ablation monitoring. *IEEE J. Biomed. Health Inform.* 24 (8), 2359–2367. <http://dx.doi.org/10.1109/JBHI.2019.2952922>.
- Besler, E., Wang, Y.C., Sahakian, A.V., 2020b. Real-time radiofrequency ablation lesion depth estimation using multi-frequency impedance with a deep neural network and tree-based ensembles. *IEEE Trans. Biomed. Eng.* 67 (7), 1890–1899. <http://dx.doi.org/10.1109/TBME.2019.2950342>.
- Burge, M.J., 2009. *Principles of Digital Image Processing*, vol. 111, Springer.
- Chang, I., 2003. Finite element analysis of hepatic radiofrequency ablation probes using temperature-dependent electrical conductivity. *Biomed. Eng. Online* 2 (1), 12. <http://dx.doi.org/10.1186/1475-925X-2-12>.
- Choi, M., Jang, M., Yoo, S.-S., Noh, G., Yoon, K., 2022. Deep neural network for navigation of a single-element transducer during transcranial focused ultrasound therapy: Proof of concept. *IEEE J. Biomed. Health Inform.* 26 (11), 5653–5664. <http://dx.doi.org/10.1109/JBHI.2022.3198650>.
- Danch-Wierzchowska, M., Borys, D., Swierniak, A., 2020. FEM-based MRI deformation algorithm for breast deformation analysis. *Biocybern. Biomed. Eng.* 40 (3), 1304–1313. <http://dx.doi.org/10.1016/j.bbe.2020.07.009>.
- de Jong, T.L., Klink, C., Moelker, A., Dankelman, J., van den Dobbelaars, J.J., 2018. Needle deflection in thermal ablation procedures of liver tumors: a CT image analysis. In: Fei, B., Webster, R.J. (Eds.), *Medical Imaging 2018: Image-Guided Procedures, Robotic Interventions, and Modeling*. In: Society of Photo-Optical Instrumentation Engineers (SPIE) Conference Series, vol. 10576, 105761L. <http://dx.doi.org/10.1117/12.2292884>.
- Dice, L.R., 1945. Measures of the amount of ecologic association between species. *Ecology* 26 (3), 297–302. <http://dx.doi.org/10.2307/1932409>.
- Finkeldey, F., Saadallah, A., Wiederkehr, P., Morik, K., 2020. Real-time prediction of process forces in milling operations using synchronized data fusion of simulation and sensor data. *Eng. Appl. Artif. Intell.* 94, 103753. <http://dx.doi.org/10.1016/j.engappai.2020.103753>.
- Fuentes, D., Cardan, R., Stafford, R.J., Yung, J., Dodd, III, G.D., Feng, Y., 2010. High-fidelity computer models for prospective treatment planning of radiofrequency ablation with in vitro experimental correlation. *J. Vasc. Interv. Radiol.* 21 (11), 1725–1732. <http://dx.doi.org/10.1016/j.jvir.2010.07.022>.
- Goodfellow, I.J., Pouget-Abadie, J., Mirza, M., Xu, B., Warde-Farley, D., Ozair, S., Courville, A., Bengio, Y., 2014. Generative adversarial networks. *arXiv:1406.2661*. URL: <https://arxiv.org/abs/1406.2661>.
- Hariharan, B., Arbeláez, P., Girshick, R., Malik, J., 2015. Hypercolumns for object segmentation and fine-grained localization. In: 2015 IEEE Conference on Computer Vision and Pattern Recognition. CVPR, pp. 447–456. <http://dx.doi.org/10.1109/CVPR.2015.7298642>.
- He, K., Zhang, X., Ren, S., Sun, J., 2016. Deep residual learning for image recognition. In: 2016 IEEE Conference on Computer Vision and Pattern Recognition. CVPR, pp. 770–778. <http://dx.doi.org/10.1109/CVPR.2016.90>.
- Henriques, Jr., F.C., 1947. Studies of thermal injury; the predictability and the significance of thermally induced rate processes leading to irreversible epidermal injury. *Arch. Pathol.* 43 (5), 489–502.
- Ho, J., Jain, A., Abbeel, P., 2020. Denoising diffusion probabilistic models. *CoRR abs/2006.11239*. [arXiv:2006.11239](https://arxiv.org/abs/2006.11239). URL: <https://arxiv.org/abs/2006.11239>.
- Ho, L.D., Min, L.J., 2018. Recent advances in the image-guided tumor ablation of liver malignancies: Radiofrequency ablation with multiple electrodes, real-time multimodality fusion imaging, and new energy sources. *Korean J. Radiol.* 19 (4), 545–559. <http://dx.doi.org/10.3348/kjr.2018.19.4.545>.
- Hoffer, E.K., Borsic, A., Patel, S.D., 2022. Validation of software for patient-specific real-time simulation of hepatic radiofrequency ablation. *Acad. Radiol.* 29 (10), e219–e227. <http://dx.doi.org/10.1016/j.acra.2021.12.018>.
- Huang, G., Liu, Z., Van Der Maaten, L., Weinberger, K.Q., 2017. Densely connected convolutional networks. In: 2017 IEEE Conference on Computer Vision and Pattern Recognition. CVPR, pp. 2261–2269. <http://dx.doi.org/10.1109/CVPR.2017.243>.
- Jaccard, P., 1912. The distribution of the flora in the alpine zone.1. *New Phytol.* 11 (2), 37–50. <http://dx.doi.org/10.1111/j.1469-8137.1912.tb05611.x>.
- Jiang, Y., Mulier, S., Wang, C., Cristiane, M., Rambo, D., Chen, F., Marchal, G., Ni, Y., Chong, S., Ni, G., 2010. Formulation of 3D finite elements for hepatic radiofrequency ablation. *Int. J. Model. Identif. Control* 9, 225–235. <http://dx.doi.org/10.1504/IJMIC.2010.032803>.
- Kath, N., Handels, H., Mastmeyer, A., 2019. Robust GPU-based virtual reality simulation of radio-frequency ablations for various needle geometries and locations. *Int. J. Comput. Assist. Radiol. Surg.* 14 (11), 1825–1835. <http://dx.doi.org/10.1007/s11548-019-02033-w>.
- Kim, Y.N., Rhim, H., Choi, D., sun Kim, Y., Lee, M.W., Chang, I., Lee, W.J., Lim, H.K., 2011. The effect of radiofrequency ablation on different organs: Ex vivo and in vivo comparative studies. *Eur. J. Radiol.* 80 (2), 526–532. <http://dx.doi.org/10.1016/j.ejrad.2009.11.011>.
- Kim, H.-J., Um, S.-H., Kang, Y.G., Shin, M., Jeon, H., Kim, B.-M., Lee, D., Yoon, K., 2023. Laser-tissue interaction simulation considering skin-specific data to predict photothermal damage lesions during laser irradiation. *J. Comput. Des. Eng.* 10 (3), 947–958. <http://dx.doi.org/10.1093/jcde/qwad033>.
- Koh, H., Park, T.Y., Chung, Y.A., Lee, J.-H., Kim, H., 2022. Acoustic simulation for transcranial focused ultrasound using GAN-based synthetic CT. *IEEE J. Biomed. Health Inform.* 26 (1), 161–171. <http://dx.doi.org/10.1109/JBHI.2021.3103387>.
- Kröger, T., Altrogge, I., Preusser, T., Pereira, P., Schmidt, D., Weihusen, A., Peitgen, H.-O., 2006. Numerical simulation of radio frequency ablation with state dependent material parameters in three space dimensions. In: *Medical Image Computing and Computer-Assisted Intervention – MICCAI 2006*. MICCAI 2006, In: Lecture Notes in Computer Science, vol. 4191, pp. 380–388. http://dx.doi.org/10.1007/11866763_47, 9.
- Kruecker, J., Xu, S., Venkatesan, A., Locklin, J.K., Amalou, H., Glossop, N., Wood, B.J., 2011. Clinical utility of real-time fusion guidance for biopsy and ablation. *J. Vasc. Interv. Radiol.* 22 (4), 515–524. <http://dx.doi.org/10.1016/j.jvir.2010.10.033>.
- Künzli, B.M., Abitabile, P., Maurer, C.A., 2011. Radiofrequency ablation of liver tumors: Actual limitations and potential solutions in the future. *World J. Hepatol.* 3 (1), 8–14. <http://dx.doi.org/10.4254/wjh.v3.i1.8>.
- Labonte, S., 1994. Numerical model for radio-frequency ablation of the endocardium and its experimental validation. *IEEE Trans. Biomed. Eng.* 41 (2), 108–115. <http://dx.doi.org/10.1109/10.284921>.
- Lanutti, M., Sharma, A., Digumarthy, S.R., Wright, C.D., Donahue, D.M., Wain, J.C., Mathisen, D.J., Shepard, J.-A.O., 2009. Radiofrequency ablation for treatment of medically inoperable stage I non-small cell lung cancer. *J. Thorac. Cardiovasc. Surg.* 137 (1), 160–166. <http://dx.doi.org/10.1016/j.jtcvs.2008.08.034>.
- Lim, H.K., 2000. Radiofrequency thermal ablation of hepatocellular carcinomas. *Korean J. Radiol.* 1 (4), 175–184. <http://dx.doi.org/10.3348/kjr.2000.1.4.175>.
- Lin, T.-Y., Dollár, P., Girshick, R., He, K., Hariharan, B., Belongie, S., 2017. Feature pyramid networks for object detection. In: 2017 IEEE Conference on Computer Vision and Pattern Recognition. CVPR, pp. 936–944. <http://dx.doi.org/10.1109/CVPR.2017.106>.
- Liu, Z., Lin, Y., Cao, Y., Hu, H., Wei, Y., Zhang, Z., Lin, S., Guo, B., 2021. Swin transformer: Hierarchical vision transformer using shifted windows. In: 2021 IEEE/CVF International Conference on Computer Vision. ICCV, IEEE Computer Society, Los Alamitos, CA, USA, pp. 9992–10002. <http://dx.doi.org/10.1109/ICCV48922.2021.00986>.
- Liu, Q., Wang, C., Li, Z., Qi, Y., Fang, J., 2024. Attention based lightweight asymmetric network for real-time semantic segmentation. *Eng. Appl. Artif. Intell.* 130, 107736. <http://dx.doi.org/10.1016/j.engappai.2023.107736>.
- Lutter, M., Ritter, C., Peters, J., 2019. Deep Lagrangian networks: Using physics as model prior for deep learning. <http://dx.doi.org/10.48550/arXiv.1907.04490>, arXiv preprint arXiv:1907.04490.
- Ma, J., He, Y., Li, F., Han, L., You, C., Wang, B., 2023. Segment anything in medical images. <http://dx.doi.org/10.48550/arXiv.2304.12306>.
- Makino, Y., Imai, Y., Igura, T., Kogita, S., Sawai, Y., Fukuda, K., Iwamoto, T., Okabe, J., Takamura, M., Fujita, N., Hori, M., Takehara, T., Kudo, M., Murakami, T., 2016. Feasibility of extracted-overlay fusion imaging for intraoperative treatment evaluation of radiofrequency ablation for hepatocellular carcinoma. *Liver Cancer* 5 (4), 269–279. <http://dx.doi.org/10.1159/000449338>.
- Mariappan, P., Weir, P., Flanagan, R., Voglreiter, P., Alhonnoro, T., Pollari, M., Moche, M., Busse, H., Futterer, J., Portugaller, H.R., Sequeiros, R.B., Kolesnik, M., 2017. GPU-based RFA simulation for minimally invasive cancer treatment of liver tumors. *Int. J. Comput. Assist. Radiol. Surg.* 12 (1), 59–68. <http://dx.doi.org/10.1007/s11548-016-1469-1>.
- Mauda-Havakuk, M., Hawken, N.M., Owen, J.W., Mikhail, A.S., Saxena, A., Karim, B., Wakim, P.G., Pritchard, W.F., Karanian, J.W., Wood, B.J., 2022. Comparative analysis of the immune response to RFA and cryoablation in a colon cancer mouse model. *Sci. Rep.* 12 (1), 18229. <http://dx.doi.org/10.1038/s41598-022-22279-w>.

- McCreedy, E.S., Cheng, R., Hemler, P.F., Viswanathan, A., Wood, B.J., McAuliffe, M.J., 2006. Radio frequency ablation registration, segmentation, and fusion tool. *IEEE Trans. Inf. Technol. Biomed.* 10 (3), 490–496. <http://dx.doi.org/10.1109/itib.2006.872076>.
- McDermott, S., Gervais, D.A., 2013. Radiofrequency ablation of liver tumors. *Semin. Interv. Radiol.* 30 (1), 49–55. <http://dx.doi.org/10.1055/s-0033-1333653>.
- McWilliams, J.P., Lee, E.W., Yamamoto, S., Loh, C.T., Kee, S.T., 2010. Image-guided tumor ablation: emerging technologies and future directions. *Semin. Interv. Radiol.* 27 (3), 302–313. <http://dx.doi.org/10.1055/s-0030-1261789>.
- Mendizabal, A., Márquez-Neila, P., Cotin, S., 2020. Simulation of hyperelastic materials in real-time using deep learning. *Med. Image Anal.* 59, 101569. <http://dx.doi.org/10.1016/j.media.2019.101569>.
- Meng, S., Zhou, Y., Gao, Z., 2024. Refined self-attention mechanism based real-time structural response prediction method under seismic action. *Eng. Appl. Artif. Intell.* 129, 107380. <http://dx.doi.org/10.1016/j.engappai.2023.107380>.
- Park, T.Y., Koh, H., Lee, W., Park, S.H., Chang, W.S., Kim, H., 2023. Real-time acoustic simulation framework for tFUS: A feasibility study using navigation system. *NeuroImage* 282, 120411. <http://dx.doi.org/10.1016/j.neuroimage.2023.120411>.
- Patterson, E.J., Scudamore, C.H., Owen, D.A., Nagy, A.G., Buczkowski, A.K., 1998. Radiofrequency ablation of porcine liver in vivo: Effects of blood flow and treatment time on lesion size. *Ann. Surg.* 227 (4), <http://dx.doi.org/10.1097/0000658-199804000-00018>.
- Peek, M.C.L., Douek, M., 2017. Ablative techniques for the treatment of benign and malignant breast tumours. *J. Ther. Ultrasound* 5, 18. <http://dx.doi.org/10.1186/s40349-017-0097-8>.
- Pennes, H.H., 1948. Analysis of tissue and arterial blood temperatures in the resting human forearm. *J. Appl. Physiol.* 1 (2), 93–122. <http://dx.doi.org/10.1152/jappl.1948.1.2.93>.
- Pérez, J.J., Nadal, E., Berjano, E., González-Suárez, A., 2022. Computer modeling of radiofrequency cardiac ablation including heartbeat-induced electrode displacement. *Comput. Biol. Med.* 144, 105346. <http://dx.doi.org/10.1016/j.compbiomed.2022.105346>.
- Rockafellar, R.T., Wets, R.J.B., 1998. *Variational Analysis*, vol. 317, Springer, pp. 117–118.
- Saha, A., Harowicz, M.R., Grimm, L.J., Kim, C.E., Ghate, S.V., Walsh, R., Mazurowski, M.A., 2018. A machine learning approach to radiogenomics of breast cancer: a study of 922 subjects and 529 DCE-MRI features. *Br. J. Cancer* 119 (4), 508–516. <http://dx.doi.org/10.1038/s41416-018-0185-8>.
- Salehi, Y., Giannacopoulos, D., 2022. PhysGNN: A physics-driven graph neural network based model for predicting soft tissue deformation in image-guided neurosurgery. *Adv. Neural Inf. Process. Syst.* 35, 37282–37296. <http://dx.doi.org/10.48550/arXiv.2109.04352>.
- Schneider, C.A., Rasband, W.S., Eliceiri, K.W., 2012. NIH image to ImageJ: 25 years of image analysis. *Nat. Methods* 9 (7), 671–675. <http://dx.doi.org/10.1038/nmeth.2089>.
- Schumann, C., Kroeger, T., Rieder, C., Hahn, H.K., 2011. GPU-based real-time approximation of the ablation zone for radiofrequency ablation. *IEEE Trans. Vis. Comput. Graphics* 17 (12), 1812–1821. <http://dx.doi.org/10.1109/TVCG.2011.207>.
- SciPy, 2023. SciPy user guide. https://docs.scipy.org/doc/scipy/reference/generated/scipy.ndimage.center_of_mass.html. (Accessed 15 November 2023).
- Shahidi, A.V., Savard, P., 1994. A finite element model for radiofrequency ablation of the myocardium. *IEEE Trans. Biomed. Eng.* 41 (10), 963–968. <http://dx.doi.org/10.1109/10.324528>.
- Shin, M., Peng, Z., Kim, H.-J., Yoo, S.-S., Yoon, K., 2023. Multivariable-incorporating super-resolution residual network for transcranial focused ultrasound simulation. *Comput. Methods Programs Biomed.* 237, 107591. <http://dx.doi.org/10.1016/j.cmpb.2023.107591>.
- Shin, M., Seo, M., Yoo, S.-S., Yoon, K., 2024. tFUSFormer: Physics-guided super-resolution transformer for simulation of transcranial focused ultrasound propagation in brain stimulation. *IEEE J. Biomed. Health Inform.* 28 (7), 4024–4035. <http://dx.doi.org/10.1109/JBHI.2024.3389708>.
- Silva, N.P., Bottiglieri, A., Conceição, R.C., O'Halloran, M., Farina, L., 2020. Characterisation of ex vivo liver thermal properties for electromagnetic-based hyperthermic therapies. *Sensors* 20 (10), 3004. <http://dx.doi.org/10.3390/s20103004>.
- Singh, S., Repaka, R., 2017. Temperature-controlled radiofrequency ablation of different tissues using two-compartment models. *Int. J. Hyperther.* 33 (2), 122–134. <http://dx.doi.org/10.1080/02656736.2016.1223890>.
- Singh, S., Repaka, R., 2018. Quantification of thermal injury to the healthy tissue due to imperfect electrode placements during radiofrequency ablation of breast tumor. *J. Eng. Sci. Med. Diagn. Ther.* 1 (1), 011002. <http://dx.doi.org/10.1115/1.4038237>.
- Sorenson, T., 1948. A method of establishing groups of equal amplitude in plant sociology based on similarity of species and its application to analyses of the vegetation on danish commons. *K. dansk. Vidensk. Selsk. Skr.* 5, 1–34.
- Trujillo, M., Berjano, E., 2013. Review of the mathematical functions used to model the temperature dependence of electrical and thermal conductivities of biological tissue in radiofrequency ablation. *Int. J. Hyperther.* 29 (6), 590–597. <http://dx.doi.org/10.3109/02656736.2013.807438>.
- Vaswani, A., Shazeer, N., Parmar, N., Uszkoreit, J., Jones, L., Gomez, A.N., Kaiser, Ł., Polosukhin, I., 2017. Attention is all you need. In: Guyon, I., Luxburg, U.V., Bengio, S., Wallach, H., Fergus, R., Vishwanathan, S., Garnett, R. (Eds.), *Advances in Neural Information Processing Systems*. Vol. 30, Curran Associates, Inc., pp. 6000–6010, URL: https://proceedings.neurips.cc/paper_files/paper/2017/file/3f5ee243547dee91fbd053c1c4a845aa-Paper.pdf.
- Vogt, P., Mariappan, P., Pollari, M., Flanagan, R., Blanco Sequeiros, R., Portugal, R.H., Fütterer, J., Schmalstieg, D., Kolesnik, M., Moche, M., 2018. RFA guardian: Comprehensive simulation of radiofrequency ablation treatment of liver tumors. *Sci. Rep.* 8 (1), 787. <http://dx.doi.org/10.1038/s41598-017-18899-2>.
- Watanabe, H., Kobayashi, Y., Fujie, M.G., 2008. Modeling the temperature dependence of thermal conductivity: Developing a system for robot-assisted RFA therapy. In: 2008 2nd IEEE RAS & EMBS International Conference on Biomedical Robotics and Biomechanics. pp. 483–488. <http://dx.doi.org/10.1109/BIOROB.2008.4762906>.
- Widmann, G., Bodner, G., Bale, R., 2009. Tumour ablation: technical aspects. *Cancer Imaging* 9 Spec No A (Special issue A), S63–7. <http://dx.doi.org/10.1102/1470-7330.2009.9026>.
- Wood, B.J., Kruecker, J., Abi-Jaoudeh, N., Locklin, J.K., Levy, E., Xu, S., Solbiati, L., Kapoor, A., Amalou, H., Venkatesan, A.M., 2010. Navigation systems for ablation. *J. Vasc. Interv. Radiol.* 21 (8, Supplement), S257–S263. <http://dx.doi.org/10.1016/j.jvir.2010.05.003>, Thermal Ablation 2010: At the Crossroads of Past Success, Current Goals, and Future Technology.
- Wu, H., Zhao, Y.-P., Tan, H.-J., 2021. A novel neural network based on dynamic time warping and Kalman filter for real-time monitoring of supersonic inlet flow patterns. *Eng. Appl. Artif. Intell.* 102, 104258. <http://dx.doi.org/10.1016/j.engappai.2021.104258>.
- Yi, H.-M., Zhang, W., Ai, X., Li, K.-Y., Deng, Y.-B., 2014. Radiofrequency ablation versus surgical resection for the treatment of hepatocellular carcinoma conforming to the milan criteria: systemic review and meta-analysis. *Int. J. Clin. Exp. Med.* 7 (10), 3150–3163.
- Zhang, Y., Zhan, X., Xiong, J., Peng, S., Huang, W., Joshi, R., Cai, Y., Liu, Y., Li, R., Yuan, K., Zhou, N., Min, W., 2018. Temperature-dependent cell death patterns induced by functionalized gold nanoparticle photothermal therapy in melanoma cells. *Sci. Rep.* 8 (1), 8720. <http://dx.doi.org/10.1038/s41598-018-26978-1>.
- Zhao, Z., Song, J., Zhu, X., Wang, J., Wu, J., Liu, Y., Nie, Z.-P., Liu, Q.H., 2013. System development of microwave induced thermo-acoustic tomography and experiments on breast tumor. *Prog. Electromagn. Res.* 134, 323–336. <http://dx.doi.org/10.2528/Pier12101604>.
- Zhu, Q., Shen, Y., Zhang, A., Xu, L.X., 2013. Numerical study of the influence of water evaporation on radiofrequency ablation. *Biomed. Eng. Online* 12 (1), 127. <http://dx.doi.org/10.1186/1475-925X-12-127>.